crystals

MDPI

Article

Numerical Simulation of Molten Pool Dynamics in Laser Deep Penetration Welding of Aluminum Alloys

Jin Peng [1,*], Hongqiao Xu [1], Xiaohong Yang [2,3,*], Xingxing Wang [1], Shuai Li [1], Weimin Long [4] and Jian Zhang [5]

1 Henan International Joint Laboratory of High-Efficiency Special Green Welding, Material College, North China University of Water Resources and Electric Power, Zhengzhou 450045, China; xuhongqiao159@126.com (H.X.); paperwxx@126.com (X.W.); lyctlishuai@163.com (S.L.)
2 Jinhua Polytechnic, Jinhua 321017, China
3 Key Laboratory of Crop Harvesting Equipment Technology of Zhejiang Province, Jinhua 321017, China
4 China Innovation Academy of Intelligent Equipment Co., Ltd., Ningbo 315700, China; brazelong@163.com
5 State Key Laboratory of Advanced Welding and Joining, Harbin Institute of Technology, Harbin 150001, China; zhangjianhit@126.com
* Correspondence: pengjin1985120@163.com (J.P.); jhyxh65@126.com (X.Y.)

Abstract: In this paper, the numerical simulation of molten pool dynamics in laser deep penetration welding of aluminum alloys was established based on the FLUENT 19.0 software. The three-dimensional transient behavior of the keyhole and the flow field of molten pool at different welding speeds were analyzed, and the influence of the welding speed on the molten pool of aluminum alloys in laser welding was obtained. The results indicated that the generation of welding spatters was directly related to the fluctuation of the diameter size in the middle of the keyhole. When the diameter in the middle of the keyhole increased by a certain extent, welding spatters occurred. When welding spatters occurred, the diameter in the middle of the keyhole became smaller. In addition, the size of the spatters at the welding speed of 9 m/min was larger than that of the spatters at the welding speeds of 3 m/min and 6 m/min. The welding spatter formed in laser deep penetration welding included: spatter created by an inclined liquid column behind the keyhole; splash created by a vertical liquid column behind the keyhole; small particles splashed in front of the keyhole. With the increase of the welding speed, the tendency of the welding spatter to form in front of the keyhole and to form a vertical liquid column behind the keyhole became weaker. When the welding speed was 9 min, only an obliquely upward liquid column appeared on the molten pool surface behind the keyhole. Compared with the welding speeds of 6 m/min and 9 m/min, the maximum flow velocity fluctuation of the molten pool at the welding speed of 3 m/min was obviously higher.

Keywords: laser welding; numerical simulation; welding speed; molten pool; keyhole

check for updates

Citation: Peng, J.; Xu, H.; Yang, X.; Wang, X.; Li, S.; Long, W.; Zhang, J. Numerical Simulation of Molten Pool Dynamics in Laser Deep Penetration Welding of Aluminum Alloys. *Crystals* **2022**, *12*, 873. https://doi.org/10.3390/cryst12060873

Academic Editor: Jiandong Wang

Received: 14 May 2022
Accepted: 15 June 2022
Published: 20 June 2022

1. Introduction

As a unique welding technology, laser welding has the advantages of high energy density and small welding deformation [1–3]. The laser welding technology is widely used in many fields, such as aerospace, automobile manufacturing, shipbuilding, and others [4–6]. Aluminum alloys have the characteristics of high thermal conductivity and low surface tension [7]. The weld defects of an aluminum alloy obtained by laser welding include porosity, undercut, etc., which would seriously affect the quality of the weld. The dynamic behavior of the weld pool has a direct impact on the formation of welding defects [8].

At present, the dynamic behavior of the molten pool is mainly studied experimentally and by numerical simulations. In experimental research, Matsunawa et al. [9,10] monitored the internal flow behavior of the molten pool in real time through an X-ray transmission high-speed camera system. Through this research, they found that the shape of the keyhole was always in a fluctuating state. When the keyhole fluctuated to a significant extent, bubbles were generated at the bottom of the keyhole. Using a modified sandwich specimen containing GG17 glass, Chen et al. [11,12] monitored keyhole morphology in real time. They found that the keyhole wall was not smooth, but rough, with a typical wrinkle structure. The bulge on the front wall of the keyhole changed the distribution of laser energy radiated on the keyhole wall, resulting in the fluctuation of vapor flow in the keyhole.

By numerical simulation, Han et al. [13] analyzed the influence of the welding driving force and found that the recoil pressure played a significant role in the welding process. When the recoil pressure was not loaded, the keyhole could not be generated in the molten pool. Rai [14] established the heat flow coupling model of laser welding and set the molten pool surface as a plane. In this model, the keyhole was in a quasi-steady state, and the temperature of the keyhole wall was the boiling point temperature of the base metal. It was found that Marangoni force could increase the width and length of the molten pool. Sohail et al. [15] studied the influence of welding heat input on the flow field of the molten pool. They found that the welding speed affected the size of the molten pool, and the higher the laser power, the more intense the flow vortex in the molten pool. Chang et al. [16] established the full penetration laser welding model of titanium alloys and found that for a welding process with low power and low speed, the fluid flow behind the keyhole was turbulent and unstable, forming a flow swirl. For higher power and higher speed welding processes, the turbulent characteristics of fluid flow were weakened, and such flow swirl would not be created. Zhao et al. [17] found that the liquid metal in front of the keyhole wall flowed to the rear of the keyhole through the bottom of the keyhole, and the liquid metal at the top of the molten pool flowed from the high-temperature area to the low-temperature area. With the progress of the welding time, the keyhole fluctuated continuously. When the depth of the keyhole suddenly decreased, welding bubbles formed at the bottom of the molten pool, which was also the main reason for the formation of pore defects. Wu et al. [18,19] established a numerical simulation model of aluminum alloy laser welding and found that welding spatter mainly occurred around the keyhole. With the accumulation of kinetic energy in the vertical direction, a bulge shape would form on the surface of the molten pool. When the momentum of the molten metal was sufficient to overcome the surface tension, a welding splash would be created. However, the flow field of the keyhole wall under different welding speeds has not been studied during laser deep penetration welding of aluminum alloys, and no research has been conducted on the correlation between keyhole, welding spatter, and molten pool flow at different welding speeds.

In this paper, a numerical simulation of molten pool dynamics in laser deep penetration welding of an aluminum alloy was established based on the FLUENT 19.0 software. The three-dimensional transient behavior of the keyhole and the flow field of the molten pool at different welding speeds were analyzed. The influence of the welding speed on the molten pool of the aluminum alloy in laser welding was obtained.

2. Mathematical Modeling

The software FLUENT 19.0 was adopted in this research work to investigate the dynamic behaviors of molten pool and keyhole. In the model, the VOF method was used to track the gas–liquid interface of the keyhole and heat transfer between different phases. The PISO algorithm was used to solve the transient flow field iteratively. A secondary development of the FLUENT 19.0 software was carried out, and the UDF (custom function) method was used to add a laser deep-penetration welding heat source and welding driving force. During the numerical simulation, the laser power was 2800 W, and the welding speed was set to 3 m/min, 6 m/min, and 9 m/min, separately.

2.1. Numerical Model and Computational Assumptions

In order to reduce the calculation time, the volume of the mathematical model (30 mm × 2.5 mm × 7.4 mm) was half the volume of the actual workpiece to be welded, as shown in Figure 1, including 511,407 nodes and 487,200 elements.

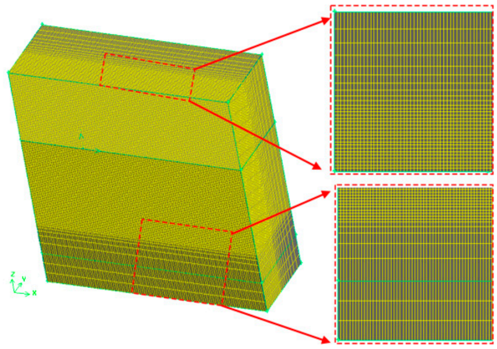

Figure 1. Calculation meshes of the numerical simulation in laser deep penetration welding.

During the modeling process, the following reasonable assumptions were adopted:

(1) The flow state of the liquid metal in the mathematical model was laminar and incompressible.
(2) The influence of the shielding gas on the temperature field and flow field of the molten pool was ignored.

2.2. Heat Source Model

When the laser power density acting on the workpiece was increased to a certain extent, the liquid metal in the molten pool was vaporized, and the keyhole formed under the action of recoil pressure. The laser rotary gauss heat source was used in the model [20].

$$q_{laser} = \frac{9\alpha_{abs}Q}{\pi R_0^2 H(1-e^3)} \exp\left[\frac{-9\left(x^2+y^2\right)}{R_0^2 \log(H/z)}\right] \quad (1)$$

where Q is the energy of the laser heat source, H is the height of the laser heat source, α_{abs} is the total coefficient of laser energy absorbed by the keyhole wall, which could be obtained from the literature [21], R_0 is the effective radius of the laser beam, which indicated that more than 95% of the total energy of the laser beam was concentrated in the region.

2.3. Governing Equations

The physical phenomena of heat and mass transfer in the laser welding process conform to three equations: continuity equation, Navier–Stokes equation, and energy conservation equation [17].

The continuity equation is:

$$\frac{\partial(\rho)}{\partial \mathrm{t}} + \frac{\partial(\rho u)}{\partial \mathrm{x}} + \frac{\partial(\rho v)}{\partial \mathrm{y}} + \frac{\partial(\rho w)}{\partial \mathrm{z}} + S_m = 0 \quad (2)$$

The energy equation is:

$$\frac{\partial(\rho \mathrm{H})}{\partial t} + \frac{\partial(\rho u \mathrm{H})}{\partial x} + \frac{\partial(\rho v \mathrm{H})}{\partial y} + \frac{\partial(\rho w \mathrm{H})}{\partial z} = \frac{\partial}{\partial x}\left(k\frac{\partial T}{\partial \mathrm{x}}\right) + \frac{\partial}{\partial y}\left(k\frac{\partial T}{\partial \mathrm{y}}\right) + \frac{\partial}{\partial z}\left(k\frac{\partial T}{\partial \mathrm{z}}\right) + S_H \quad (3)$$

The Navier–Stokes equation along different axes is described as:

$$\frac{\partial(\rho \mathrm{u})}{\partial t} + \frac{\partial(\rho \mathrm{uu})}{\partial x} + \frac{\partial(\rho \mathrm{uv})}{\partial y} + \frac{\partial(\rho \mathrm{uw})}{\partial z} = \frac{\partial}{\partial x}\left(u\frac{\partial u}{\partial x}\right) + \frac{\partial}{\partial y}\left(u\frac{\partial u}{\partial y}\right) + \frac{\partial}{\partial z}\left(u\frac{\partial u}{\partial z}\right) - \frac{\partial P}{\partial x} + S_x \quad (4)$$

$$\frac{\partial(\rho v)}{\partial t}+\frac{\partial(\rho uv)}{\partial x}+\frac{\partial(\rho vv)}{\partial y}+\frac{\partial(\rho vw)}{\partial z}=\frac{\partial}{\partial x}\left(u\frac{\partial v}{\partial x}\right)+\frac{\partial}{\partial y}\left(u\frac{\partial v}{\partial y}\right)+\frac{\partial}{\partial z}\left(u\frac{\partial v}{\partial z}\right)-\frac{\partial P}{\partial y}+S_y \tag{5}$$

$$\frac{\partial(\rho w)}{\partial t}+\frac{\partial(\rho uw)}{\partial x}+\frac{\partial(\rho vw)}{\partial y}+\frac{\partial(\rho ww)}{\partial z}=\frac{\partial}{\partial x}\left(u\frac{\partial w}{\partial x}\right)+\frac{\partial}{\partial y}\left(u\frac{\partial w}{\partial y}\right)+\frac{\partial}{\partial z}\left(u\frac{\partial w}{\partial z}\right)-\frac{\partial P}{\partial z}+S_z \tag{6}$$

where u, v, and w denote different components of velocity; ρ, P, H, k, and μ are the density, pressure, enthalpy, thermal conductivity, and viscosity, respectively; S_m, S_x, S_y, S_z, and S_H indicate the source terms of the continuity equation, momentum equations, and energy equation.

2.4. Driving Force

When the workpiece irradiated by the laser beam was welded, the workpiece surface melted and evaporated, resulting in recoil pressure. With the welding time increasing, the molten metal was discharged under the action of recoil pressure, thus forming a keyhole. The mathematical expression of recoil pressure is as follows [22].

$$\mathrm{P}_r = AB_0T_s^{-\frac{1}{2}}\exp\left(-\frac{U}{T_s}\right) \tag{7}$$

where A is a coefficient related to atmospheric pressure, and B_0 is the vaporization constant.

Surface tension is closely related to temperature. The mathematical expression of surface tension is as follows:

$$\delta(\mathrm{T}) = \delta_0 + A_\delta(T - T_m) \tag{8}$$

where δ_0 is the surface tension at T_m, A_δ is the temperature coefficient of surface tension, and T_m is the reference temperature.

In the process of laser welding, different levels of thermal buoyancy were produced due to the different temperatures in various positions of the molten pool. The mathematical expression of thermal buoyancy in the molten pool is as follows:

$$F_b = \rho g\beta(T - T_m) \tag{9}$$

where g is the gravity, and β is the coefficient of thermal expansion for the material.

The physical and thermal properties of the 6056 aluminum alloy in modeling are summarized in Table 1.

Table 1. Physical and thermal properties of the 6056 aluminum alloy.

Property	Symbol	Unite	Value
Solid density	ρ_s	Kg m^{-3}	2720
Liquid density	ρ_l	Kg m^{-3}	2590
Solidus temperature	T_s	K	860
Liquidus temperature	T_L	K	917
Boiling temperature	T_g	K	2740
Latent heat of fusion	L_m	J kg^{-1}	3.87×10^5
Latent heat of the vapor	L_v	J kg^{-1}	1.08×10^7
Thermal expansion coefficient	β_k	K^{-1}	1.92×10^{-5}
Convective heat transfer coefficient	h_0	W K^{-1} m^{-2}	15
Surface tension	δ_0	N m^{-1}	0.914
Surface tension gradient	A_δ	N m^{-1} K^{-1}	-3.5×10^{-4}
Radiation emissivity	ε	-	0.08
Ambient temperature	T_{ref}	K	300

The thermo-physical properties dependent on the temperature are as follows

$$C_p\left(Jkg^{-1}K^{-1}\right) = \begin{cases} -0.001 \times T^2 + 1.1609 \times \mathrm{T} + 267.71 & 300 < T \leq 573 \\ 0.0009 \times T^2 - 0.3901 \times T + 514.45 & 573 < T \leq 913 \\ -0.0009 \times T^2 + 0.5832 \times T + 435.14 & 913 < T \leq 2740 \end{cases} \quad (10)$$

$$\mathrm{k}\left(Wm^{-1}K^{-1}\right) = \begin{cases} -0.0001 \times T^2 - 0.0697 \times \mathrm{T} + 95.334 & 300 < T \leq 860 \\ -0.0048 \times T^2 + 9.2812 \times T - 4275.6 & 860 < T \leq 917 \\ -0.00001 \times T^2 + 0.0582 \times T + 148.74 & 917 < T \leq 2740 \end{cases} \quad (11)$$

$$\mu\left(\mathrm{kg}m^{-1}K^{-1}\right) = \begin{cases} 1 \times 10^{-7} \times T^2 - 0.0002 \times \mathrm{T} + 0.1202 & 897 < T \leq 937 \\ 2 \times 10^{-11} \times T^2 - 5 \times 10^{-7} \times T + 0.0038 & 937 < T \leq 2650 \\ -6 \times 10^{-8} \times T^2 + 0.0003 \times T - 0.4151 & 2650 < T \leq 2720 \end{cases} \quad (12)$$

3. Results and Discussion

3.1. Comparison between the Calculated and the Experimental Result

Figure 2 shows the comparison between the experimental weld seam cross section and the simulated molten pool at a welding speed of 3 m/min. In the experimental results, the penetration depth was about 2.4 mm, and the bead width was 2.6 mm. It was found that the shape and dimensions of the numerically obtained weld pool were in good agreement with those obtained experimentally.

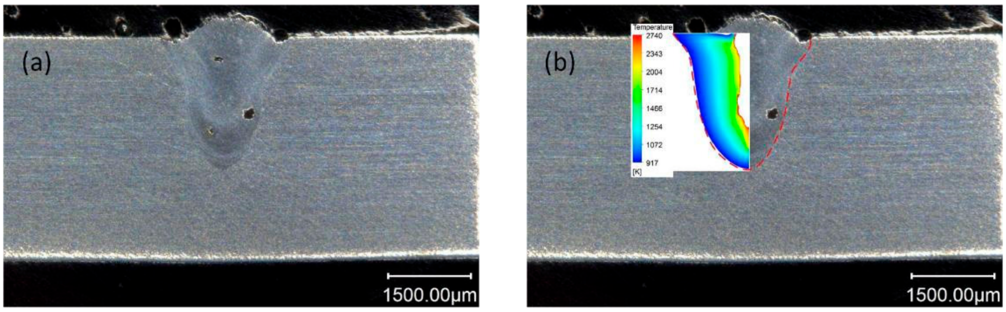

Figure 2. Comparison of the experimental weld seam with the simulated molten pool. (**a**) the experimental weld seam cross section at a welding speed of 3 m/min; (**b**)the simulated molten pool at a welding speed of 3 m/min.

3.2. Three-Dimensional Transient Behavior of Keyhole

In this paper, the three-dimensional morphology of the keyhole and the flow field of the keyhole wall at different welding speeds were analyzed. Figures 3–5 show the three-dimensional morphology of the keyhole and the flow field of keyhole wall at welding speeds of 3 m/min, 6 m/min, and 9 m/min. Through comparison, it was found that the keyhole depth gradually decreased with the increase of the welding speed. The main reason was that after increasing the welding speed, the heat input acting on the welding workpiece per unit time decreased. When the welding speed was 3 m/min, the lower part of the keyhole was closed (Figure 3d); when the welding speed was 6 m/min (Figure 4) and 9 m/min (Figure 5), the keyhole was not closed. Moreover, with the increase of the welding speed, the fluctuation of the three-dimensional shape of the keyhole decreased gradually. This shows that with the increase of the welding speed, the stability of the keyhole was steadily improved.

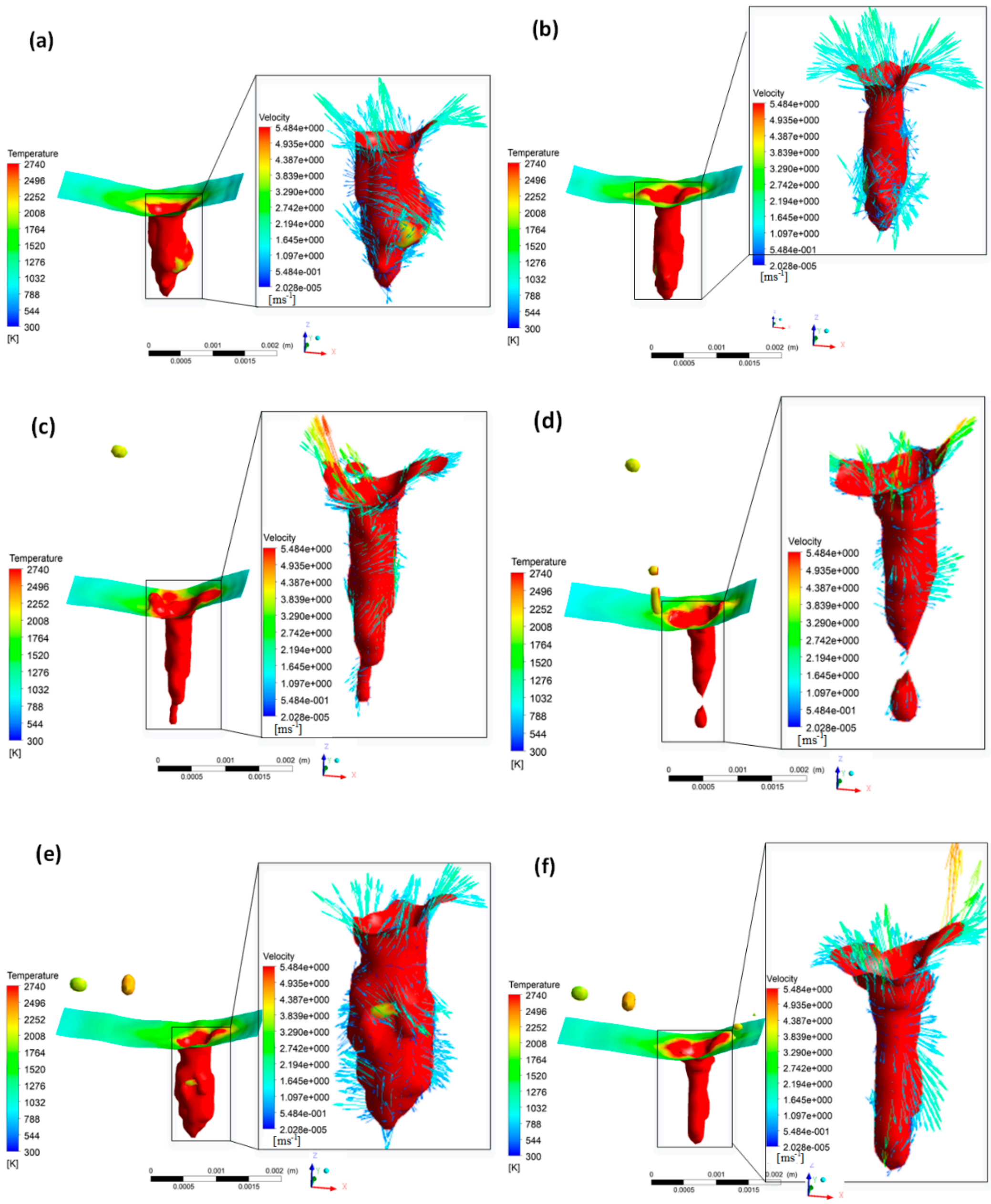

Figure 3. Three-dimensional transient behavior of the keyhole when the welding speed was 3 m/min: (**a**) *t* = 24 ms, (**b**) *t* = 25 ms, (**c**) *t* = 28.5 ms, (**d**) *t* = 28.8 ms, (**e**) *t* = 46.3 ms, (**f**) *t* = 46.8 ms.

The generation of welding spatters was directly related to the fluctuation of the size in the middle of the keyhole. When the diameter in the middle of the keyhole increased to a certain value, welding spatters occurred. When welding spatters occurred, the diameter in the middle of the keyhole became smaller. When the welding speed was 3 m/min, the diameter in the middle of the keyhole was 0.69 mm at *t* = 24 ms (Figure 3a). After welding spatters occurred, the diameter in the middle of the keyhole was 0.31 mm at *t* = 28.8 ms (Figure 3d). When the welding speed was 6 m/min, the diameter in the middle of the keyhole was 0.46 mm at *t* = 18.2 ms (Figure 4c). After welding spatters occurred, the diameter in the middle of the keyhole was 0.39 mm at *t* = 18.5 ms (Figure 4f). When the welding speed was 9 m/min, the diameter in the middle of the keyhole was 0.49 mm at *t* = 12.5 ms (Figure 5d). After welding spatters occurred, the diameter in the middle of the keyhole was 0.33 mm at *t* = 18.5 ms *t* = 13.2 ms (Figure 5e).

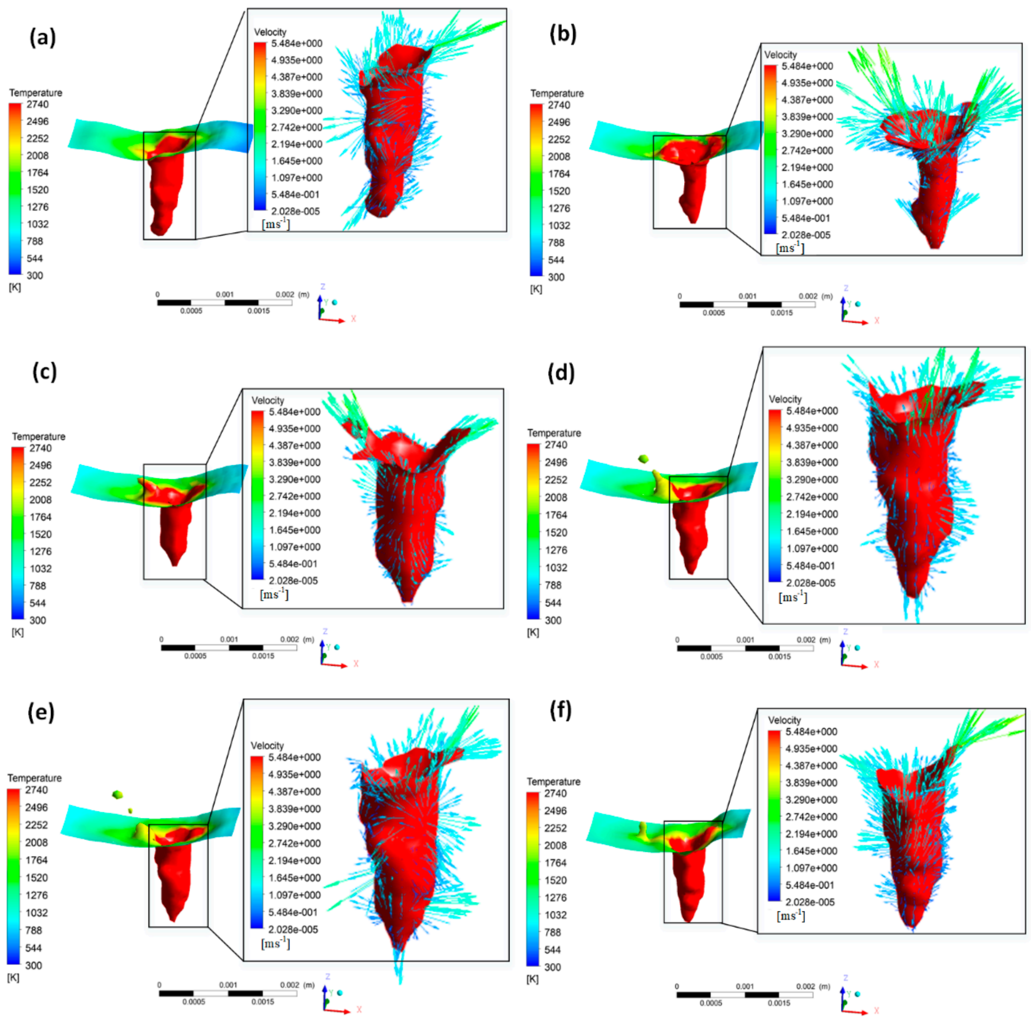

Figure 4. Three-dimensional transient behavior of the keyhole when the welding speed was 6 m/min: (**a**) t = 17 ms, (**b**) t = 18.1 ms, (**c**) t = 18.2 ms, (**d**) t = 18.3 ms, (**e**) t = 18.4 ms, (**f**) t = 18.5 ms.

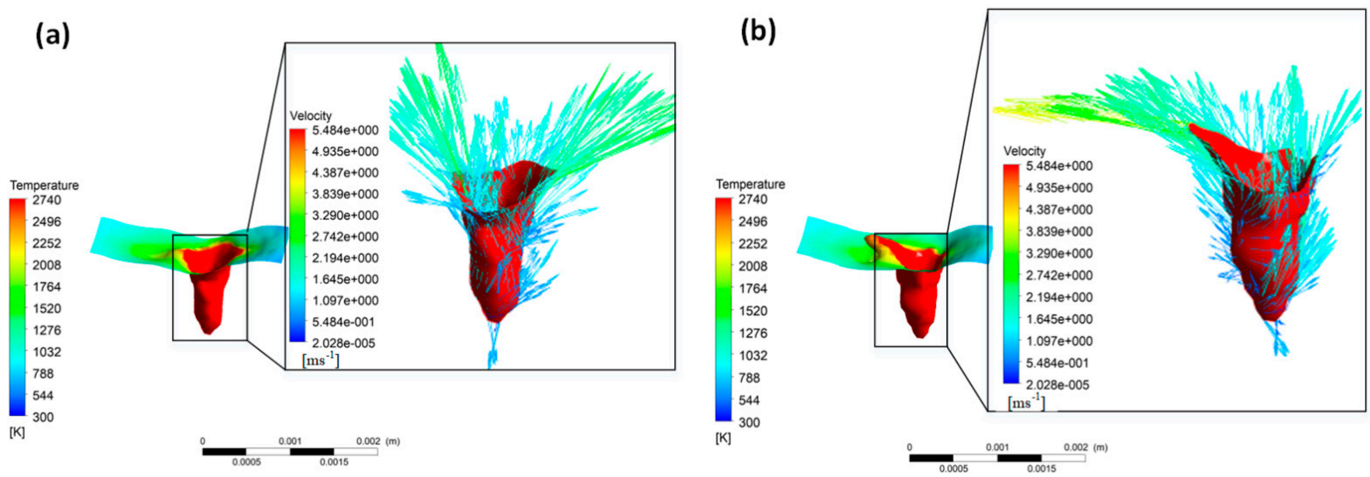

Figure 5. *Cont.*

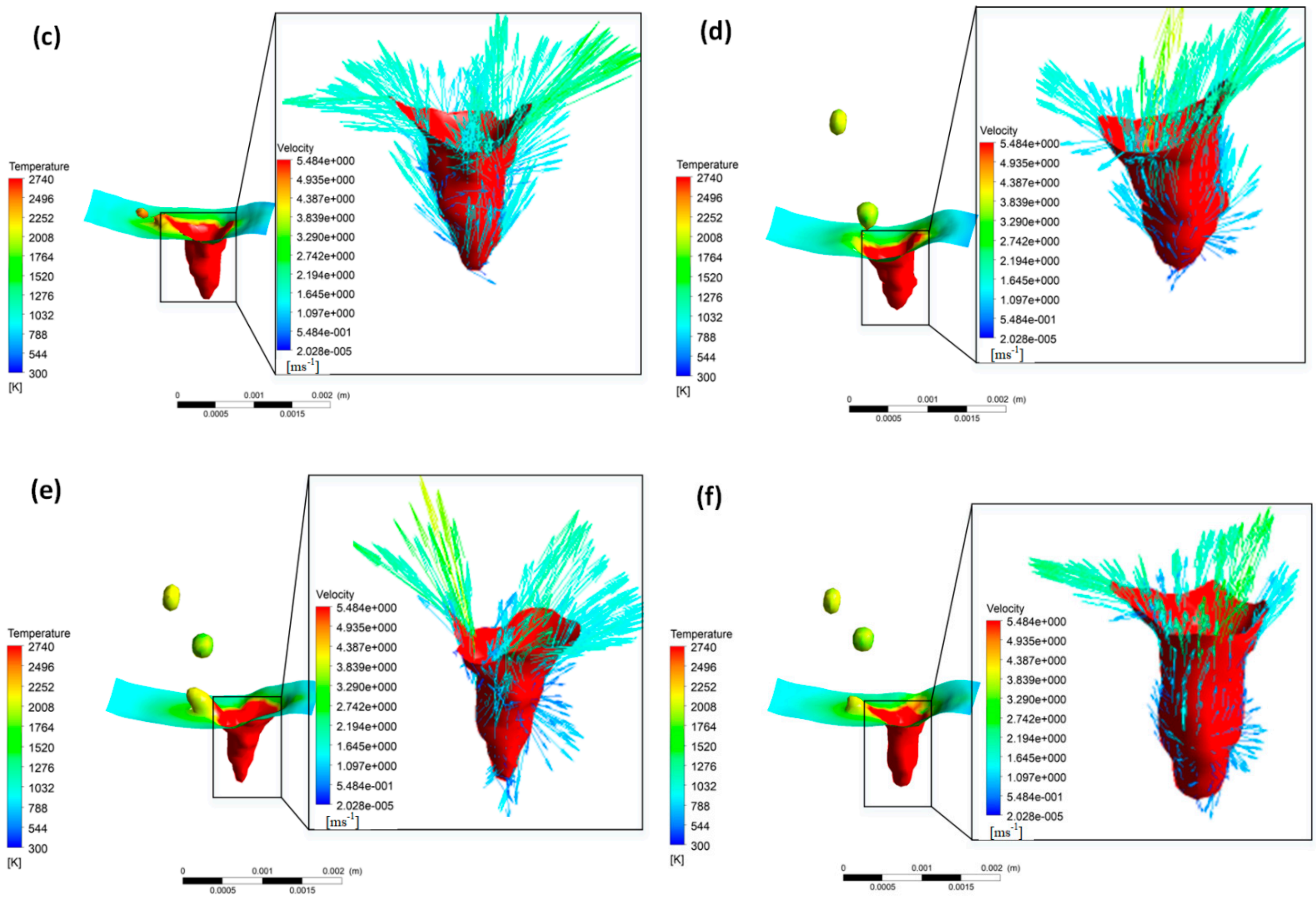

Figure 5. Three-dimensional transient behavior of the keyhole when the welding speed was 9 m/min: (**a**) t = 7.6 ms, (**b**) t = 7.9 ms, (**c**) t = 8 ms, (**d**) t = 12.5 ms, (**e**) t = 13.2 ms, (**f**) t = 13.4 ms.

When the welding speed was 3 m/min, the direction of the flow field on the wall of the keyhole was more complex. The fluid flow at the opening of the keyhole showed an upward trend, while in the middle and lower part of the keyhole, the flow field on the wall of the keyhole at different welding times was more complex and did not follow a unified law. When the welding speed was 6 m/min, the complexity of the flow field direction on the keyhole wall was reduced. The fluid flow at the opening of the keyhole and in the middle of the keyhole showed an upward trend. When the welding speed was 9 m/min, the direction of the flow field on the keyhole wall was relatively uniform and basically showed an upward trend along the keyhole wall.

3.3. Flow Field of the Molten Pool

The flow field of the molten pool at different welding speeds was further studied. Figures 6–8 show the flow field of the molten pool at welding speeds of 3 m/min, 6 m/min, and 9 m/min, separately. When the welding speed was 3 m/min, the flow in the molten pool was complex, and a clockwise flow vortex appeared behind the bottom of the keyhole. When the welding speed was 6 m/min, the clockwise flow vortex behind the bottom of the keyhole appeared only in the conditions shown in Figure 7a, and exhibited a flow trend from the bottom of the molten pool to the top of the molten pool behind the keyhole (as shown in Figure 7b–f). When the welding speed was 9 m/min, the clockwise flow vortex behind the bottom of the keyhole disappeared, and the flow behind the keyhole from the bottom of the molten pool to the top of the molten pool appeared in the molten pool at different welding times. When the welding speed was 3 m/min, 6 m/min, and 9 m/min, the flow from the keyhole opening to the edge of the molten pool appeared on the surface of the molten pool, which was mainly caused by the Marangoni flow force. The liquid metal near the keyhole opening had a high temperature and a low surface tension. In contrast, the liquid metal at the edge of the molten pool had a low temperature and a high surface tension; therefore, this flow behavior appeared.

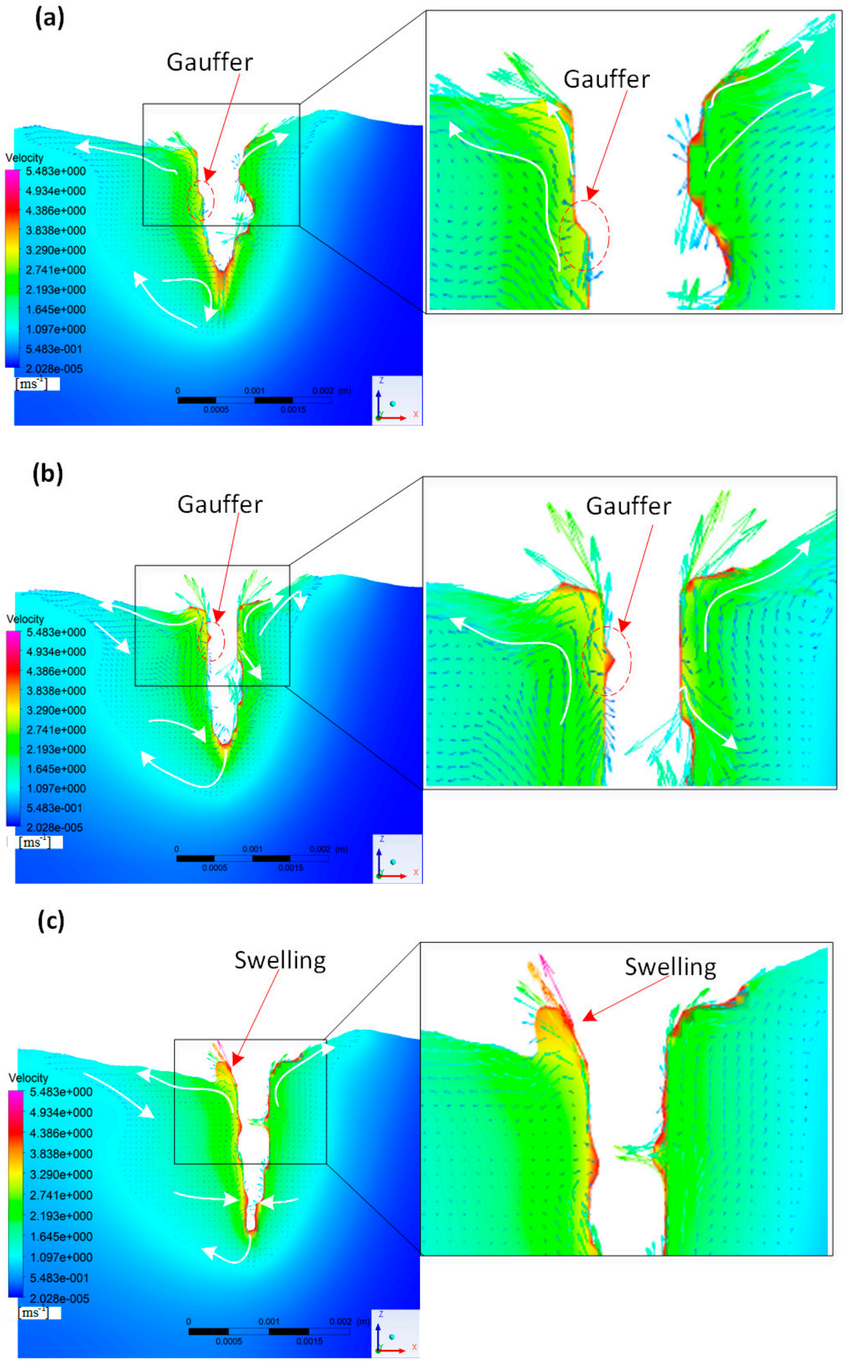

Figure 6. *Cont.*

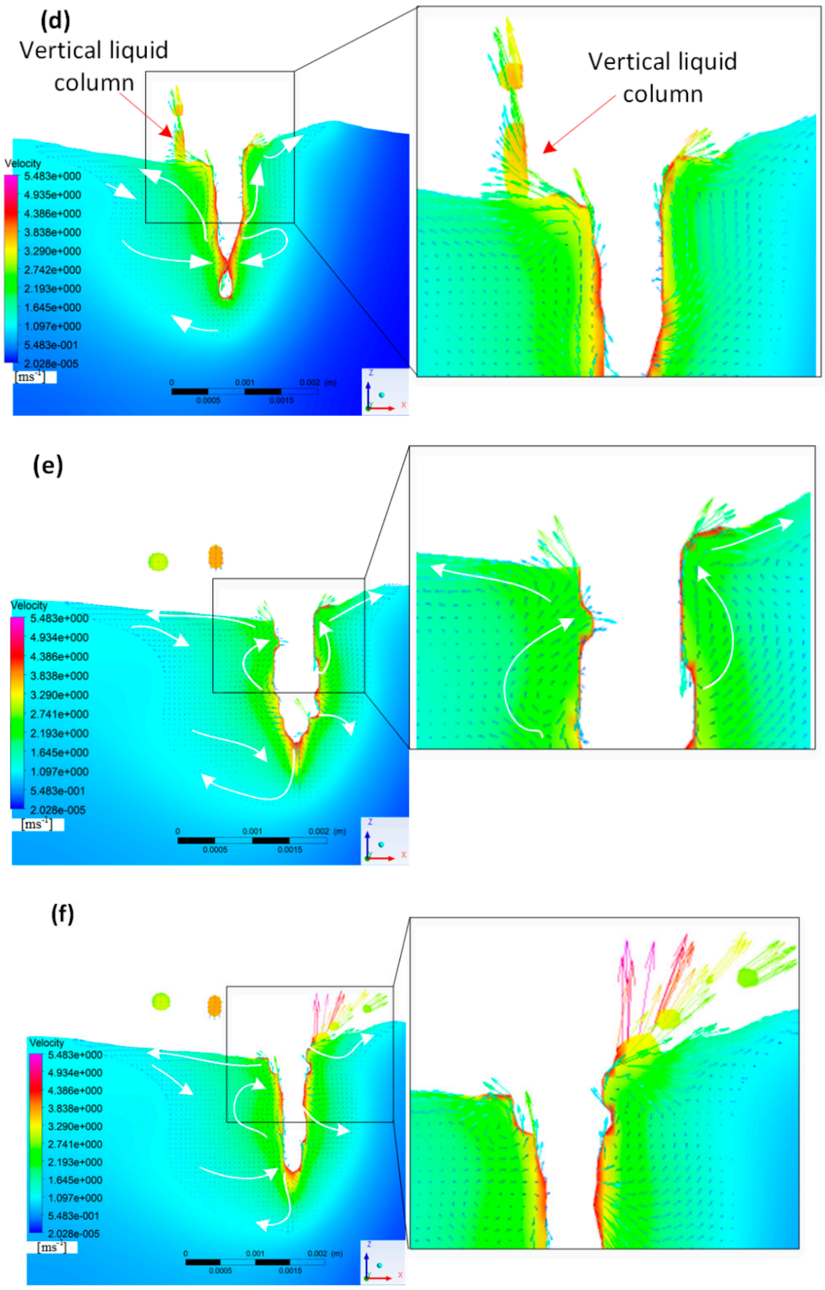

Figure 6. Flow field of the molten pool when the welding speed was 3 m/min: (**a**) t = 24 ms, (**b**) t = 25 ms, (**c**) t = 28.5 ms, (**d**) t = 28.8 ms, (**e**) t = 46.3 ms, (**f**) t = 46.8 ms.

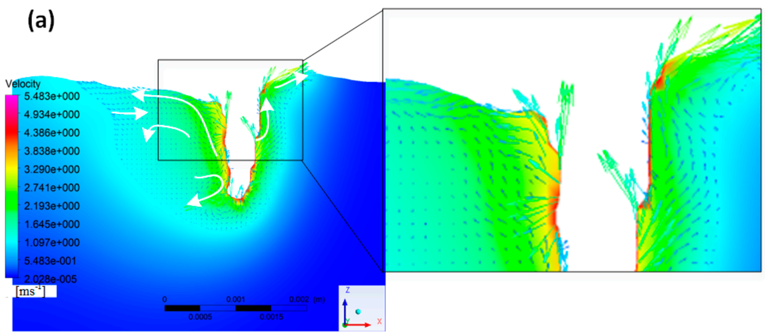

Figure 7. *Cont.*

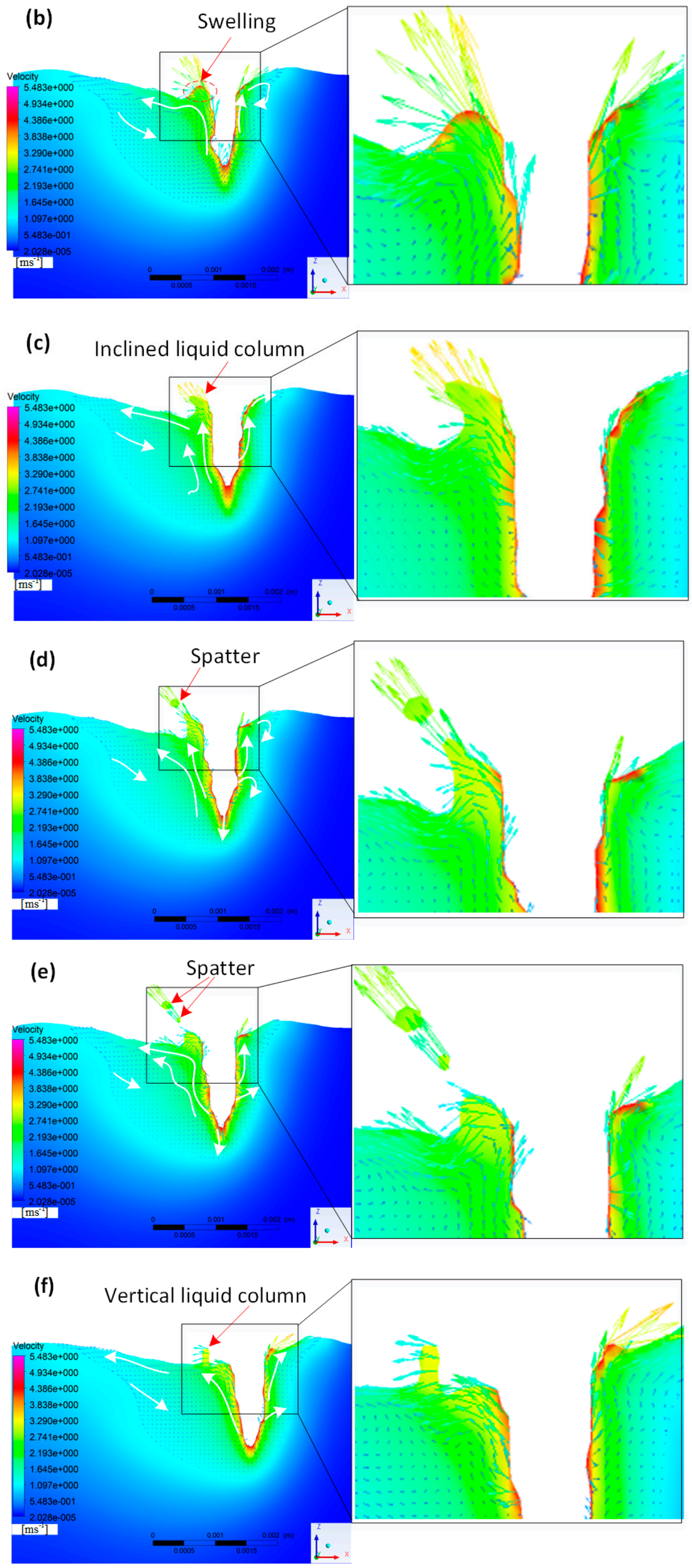

Figure 7. Flow field of molten pool when the welding speed was 6 m/min:(**a**) t = 17 ms, (**b**) t = 18.1 ms, (**c**) t = 18.2 ms, (**d**) t = 18.3 ms, (**e**) t = 18.4 ms, (**f**) t = 18.5 ms.

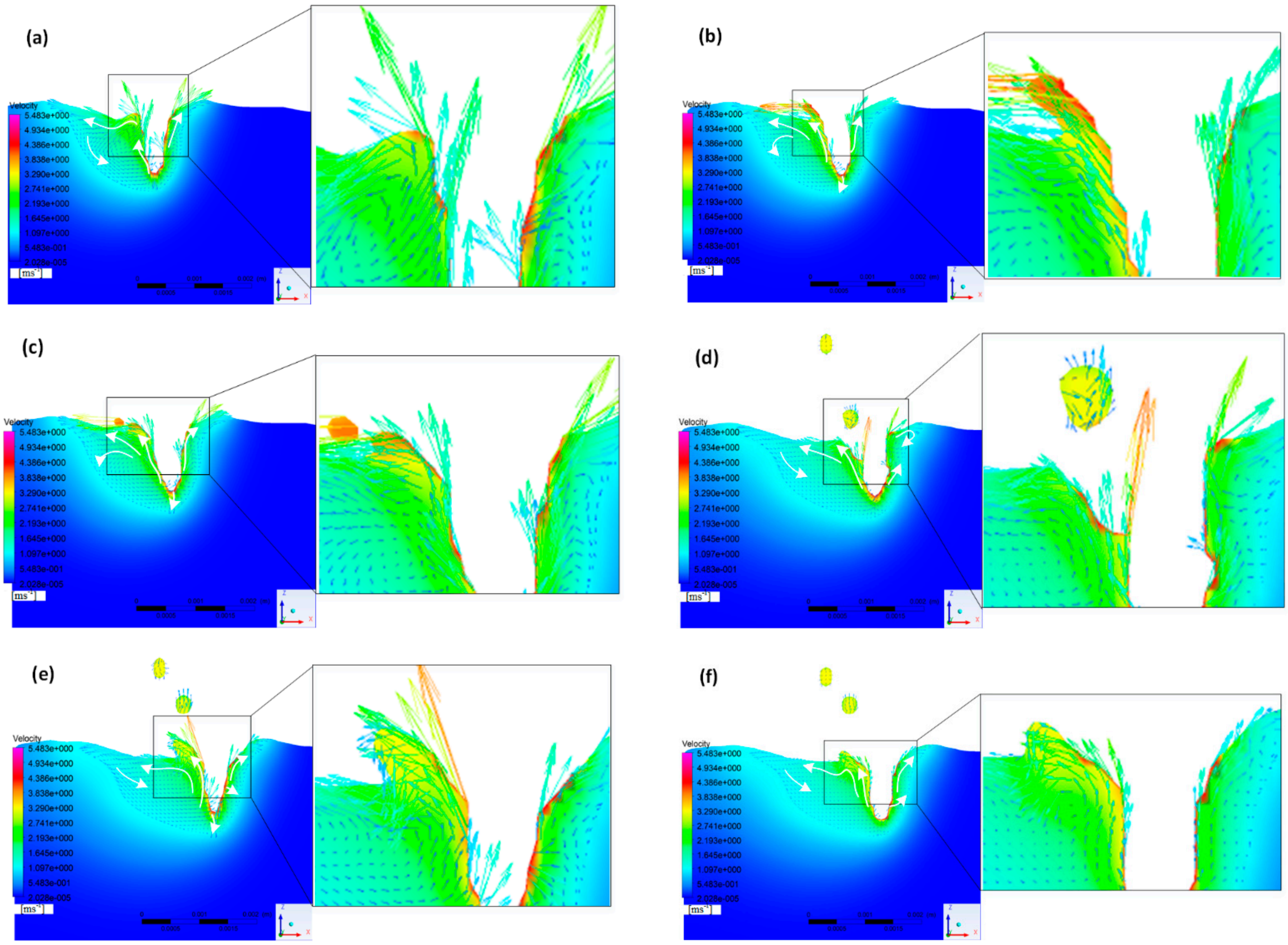

Figure 8. Flow field of molten pool when the welding speed was 9 m/min: (**a**) t = 7.6 ms, (**b**) t = 7.9 ms, (**c**) t = 8 ms, (**d**) t = 12.5 ms, (**e**) t = 13.2 ms, (**f**) t = 13.4 ms.

Figures 9–11 show the velocity contour of the molten pool at welding speeds of 3 m/min, 6 m/min and 9 m/min, separately. When the welding speed was 3 m/min, welding spatters would be generated in the rear of the keyhole (Figure 9d) and on the surface of the molten pool in front of the keyhole (Figure 9f). However, the maximum flow speed of the molten pool in front of the keyhole was significantly higher than that behind the keyhole. This was because the laser directly acted on the front wall of the keyhole during the welding process, resulting in recoil pressure. Under the action of recoil pressure on the front wall of the keyhole, the maximum flow velocity of the molten pool in front of the keyhole was higher. When the welding speed was 6 m/min and 9 m/min, the welding spatters appeared on the surface of the molten pool behind the keyhole, but there were no welding spatters on the surface of the molten pool in front of the keyhole. This was because, with the increase of the welding speed, the thickness of the molten pool in front of the keyhole wall decreased, so the probability of having welding spatters in the molten pool in front of the keyhole wall decreased. When the welding speed was 3 m/min and 6 m/min, there was a liquid column perpendicular to the surface of the molten pool behind the keyhole (Figures 9d and 10f). When the welding speed was 9 m/min, there was no liquid column perpendicular to the molten pool surface, and only an obliquely upward liquid column appeared on the molten pool surface behind the keyhole (Figure 11b,c,e,f). The size of spatters at the welding speed of 9 m/min was larger than that at welding speeds of 3 m/min and 6 m/min.

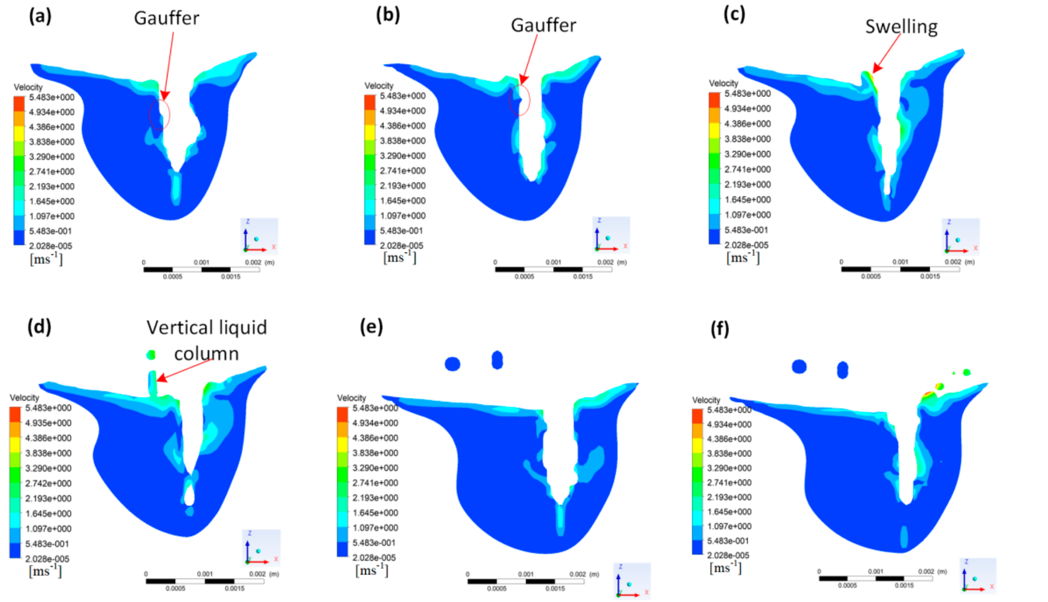

Figure 9. Velocity contour of the molten pool when the welding speed was 3 m/min: (**a**) t = 24 ms, (**b**) t = 25 ms, (**c**) t = 28.5 ms, (**d**) t = 28.8 ms, (**e**) t = 46.3 ms, (**f**) t = 46.8 ms.

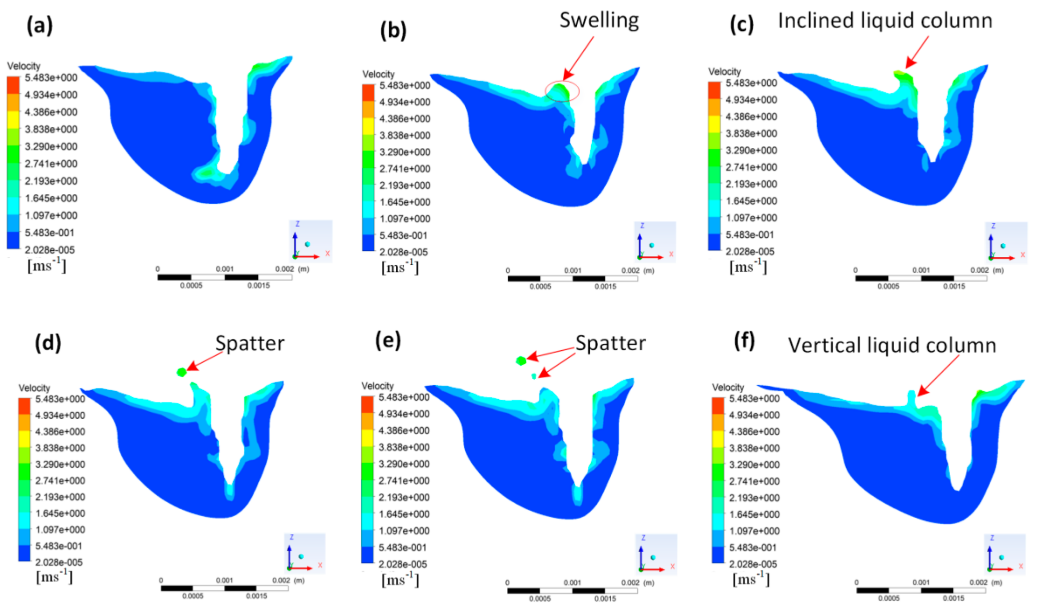

Figure 10. Velocity contour of the molten pool when the welding speed was 6 m/min: (**a**) t = 17 ms, (**b**) t = 18.1 ms, (**c**) t = 18.2 ms, (**d**) t = 18.3 ms, (**e**) t = 18.4 ms, (**f**) t = 18.5 ms.

Figure 12 shows the relationship between laser source displacement and maximum velocity of the molten pool. It shows that, compared with the results at the welding speeds of 6 m/min and 9 m/min, the maximum flow velocity fluctuation of the molten pool at the welding speed of 3 m/min was obviously higher. This was mainly because when the welding speed was 3 m/min, the laser energy density was high, and metal evaporation was intense. When the welding speed was low, the fluctuation of the molten pool was large, so the keyhole could be closed easily (Figure 3d). The maximum value of the maximum flow velocity in the molten pool at the welding speed of 3 m/min was 10.25 m/s, and the minimum value was 3.64 m/s. When the welding speed was 6 m/min, the maximum value of the maximum flow velocity in the molten pool was 7.51 m/s, and the minimum value was 3.11 m/s. When the welding speed was 9 m/min, the maximum value of the maximum flow velocity in the molten pool was 7 m/s, and the minimum velocity was 3.57 m/s.

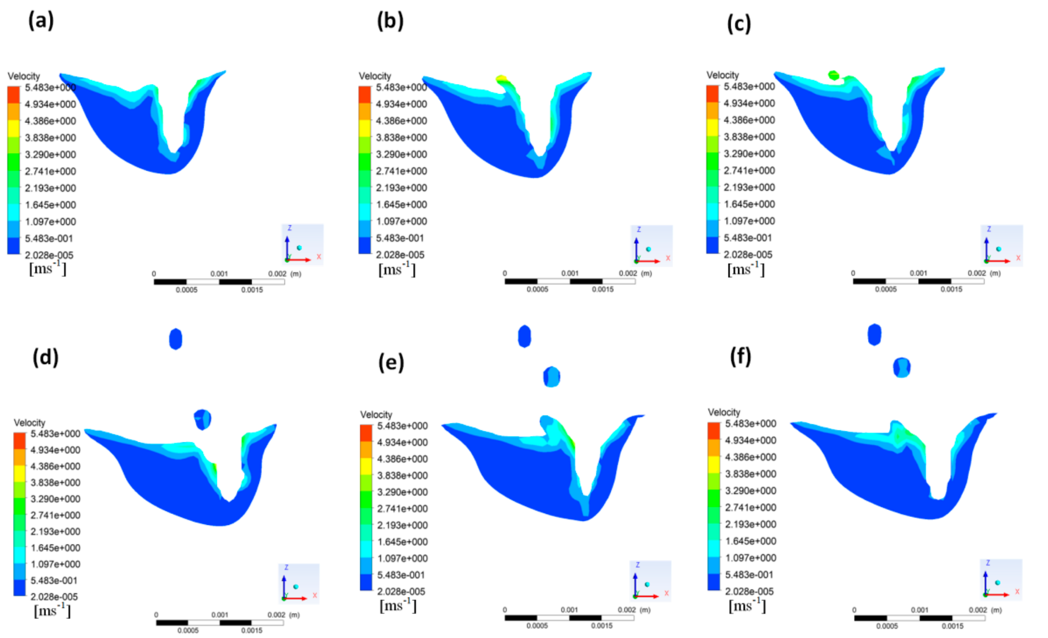

Figure 11. Velocity contour of the molten pool when the welding speed was 9 m/min: (**a**) t = 7.6 ms, (**b**) t = 7.9 ms, (**c**) t = 8 ms, (**d**) t = 12.5 ms, (**e**) t = 13.2 ms, (**f**) t = 13.4 ms.

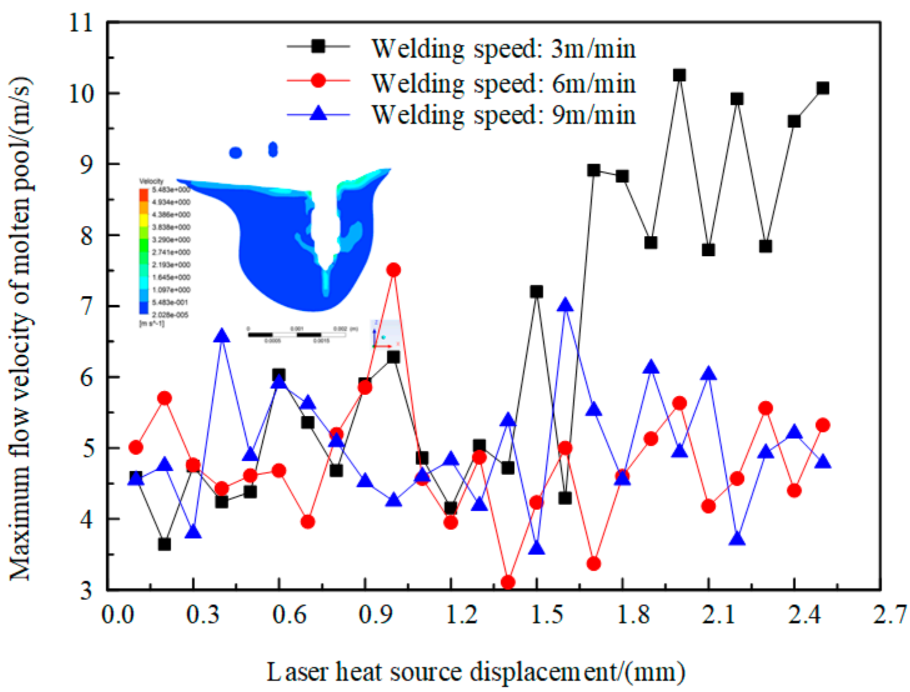

Figure 12. Relationship between laser source displacement and maximum flow velocity of the molten pool.

In laser deep penetration welding of aluminum alloys, as the welding speed gradually increases, the vortices in the rear molten pool disappear, and the melt shows an increased tendency to upward movement. This phenomenon is beneficial to improve the stability of the molten pool and reduce the porosity of the weld bead [23]. In keyhole mode laser welding, the keyhole is basically unstable. When the keyhole progressively closed because of its instability, the laser beam strongly interacted with the molten metal at the closing area and opened the keyhole again by high recoil pressure, as shown in Figure 13. Thus, the keyhole oscillated in the radial direction while it was maintained during laser deep penetration welding. When the diameter in the middle of the keyhole increased to a certain value, it caused welding spatter, as shown in Figures 3–5.

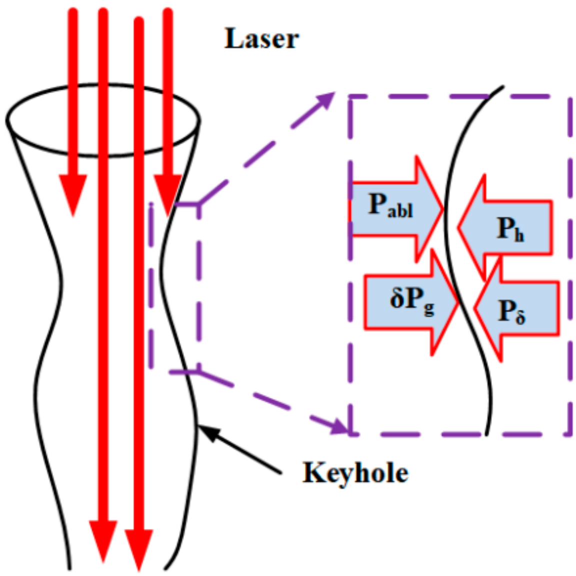

Figure 13. Force acting on the keyhole wall.

When the keyhole is stable, the formula of the force acting on the keyhole wall is as follows:

$$P_{abl} + \delta P_g = P_\sigma + P_h \tag{13}$$

where P_{abl} is the recoil pressure (N/m^2), δP_g is the excess vapor pressure ($\delta P_g = P_v - P_0$, P_v: vapor pressure, P_0: atmospheric pressure) (N/m^2), P_σ is the surface tension pressure, and P_h is the hydrostatic pressure (N/m^2). Pressure terms on the left side act to open the keyhole and those of the right side act to close the keyhole.

In keyhole (KH) mode laser welding, the dynamic fluctuation of the keyhole directly affects the stability of the molten pool. The basic phenomenon that is at the origin of KH formation is the recoil pressure that pushes the liquid generated during the initial stage of laser deep penetration welding. A scheme of the longitudinal section of a keyhole in laser deep penetration welding is shown in Figure 14. AThen incident beam has uniform intensity I_0 and diameter D. V_d is the 'drilling velocity'.

The penetration depth L is described by the following Equation [24]:

$$\mathrm{L} \approx kI_0A_0D/V_w = (4A_0k/\pi)P/(DV_W) \tag{14}$$

where P is the incident laser power, A_0 is the absorptivity under normal incidence, and k is representative of some energy balance of the process that depends mainly on the workpiece material. According to Equation (14), the penetration depth scaled as $1/V_w$.

The keyhole front wall (KFW) inclination α is given by a rather simple relation:

$$\mathrm{tg}\alpha \approx V_W/(kI_0A_0) \tag{15}$$

At a low welding speed, the inclination angle of the KFW is very small. The keyhole is quite vertical. It is also rather unstable and continuously re-opens, and consequently the metal vapor plume is mainly ejected upwards. Under these conditions, this vapor plume has much less impact on the keyhole rear wall (KRW) and interacts mainly by its friction effect along the KH walls. The absorbed intensity I_{abs} on the keyhole front is obtained by Equation (16):

$$\mathrm{I}_{abs} = \mathrm{I}_0 A_0 \sin\alpha = V_W / k \tag{16}$$

It was found that the absorbed intensity on the keyhole front was totally independent of the incident intensity; it only depended on the welding speed. Therefore, the evaporation recoil pressure on the KFW increased with the increase of the welding speed. At the same time, the impact of vapor on the KRW increased with the increase of the welding speed.

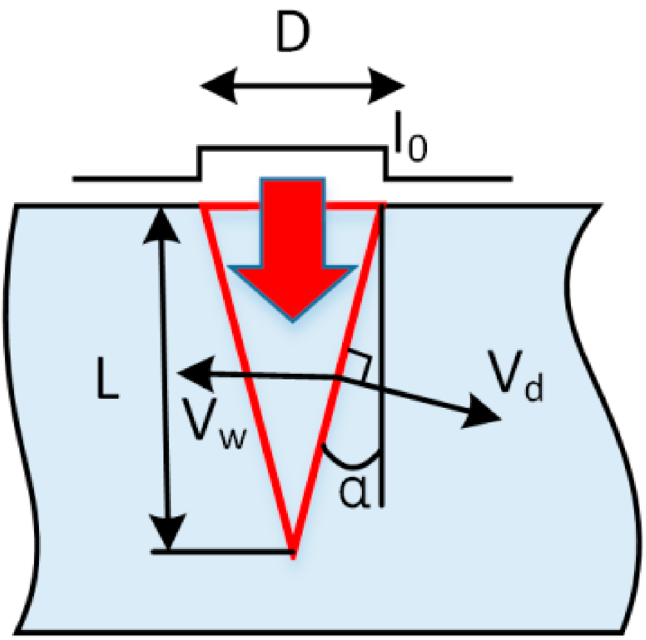

Figure 14. Scheme of the longitudinal section of a keyhole in laser deep penetration welding.

4. Conclusions

1. The generation of welding spatters was directly related to the fluctuation of the diameter size in the middle of the keyhole. When the diameter in the middle of the keyhole increased to a certain extent, welding spatters occurred. When welding spatters occurred, the diameter in the middle of the keyhole became smaller, and the size of spatters at the welding speed of 9 m/min was larger than that at welding speeds of 3 m/min and 6 m/min.
2. The welding spatter forms of laser deep penetration welding included: spatter formed by an inclined liquid column behind the keyhole; splash created by a vertical liquid column behind the keyhole; small particles splashed in front of the keyhole. With the increase of the welding speed, the tendency of the welding spatter to form in front of the keyhole and form a vertical liquid column behind the keyhole became weaker. When the welding speed was 9 m/min, only an obliquely upward liquid column appeared on the molten pool surface behind the keyhole.
3. Compared with the welding speeds of 6 m/min and 9 m/min, the maximum flow velocity fluctuation of the molten pool at the welding speed of 3 m/min was obviously higher. The maximum value of the maximum flow velocity in the molten pool was reduced from 10.25 m/s to 7 m/s as the welding speed increased from 3 m/min to 9 m/min.
4. With the increase of the welding speed, the complexity of the keyhole wall flow field decreased. When the welding speed was 9 m/min, the direction of the flow field on the keyhole wall was relatively uniform and showed an upward trend along the keyhole wall.

Author Contributions: Conceptualization, J.P. and X.Y.; methodology, J.P. and H.X.; software, J.P.; validation, J.P., X.W. and S.L.; formal analysis, J.P. and W.L.; investigation, J.P. and X.Y.; resources, J.P. and H.X.; data curation, J.P. and X.Y.; writing—original draft preparation, J.P. and H.X.; writing—review and editing, J.P.; visualization, J.P. and J.Z.; supervision, J.P. and X.Y.; project administration, J.P. and H.X.; funding acquisition, J.P. and X.Y. All authors have read and agreed to the published version of the manuscript.

Funding: This research received no external funding.

Institutional Review Board Statement: Not applicable.

Informed Consent Statement: Not applicable.

Data Availability Statement: Not applicable.

Acknowledgments: This work was supported by the National Natural Science Foundation of China (52071165), the Henan Province Key R & D and Promotion Project (Science and Technology Research) (222102220082), the Henan Postdoctoral Research Project (202003076), the Henan Excellent Youth Fund Project (202300410268), the Scientific and technological innovation talents in Colleges and universities in Henan Province (22HASTIT026) Project of the Research Foundation for High-level Talents in North China University of Water Resources and Electric Power (201705006).

Conflicts of Interest: The authors declare no conflict of interest.

References

1. Frostevarg, J. Factors affecting weld root morphology in laser keyhole welding. *Opt. Lasers Eng.* **2018**, *101*, 89–98. [CrossRef]
2. Atabaki, M.M.; Yazdian, N.; Ma, J.; Kovacevic, R. High power laser welding of thick steel plates in a horizontal butt joint configuration. *Opt. Laser Technol.* **2016**, *83*, 1–12. [CrossRef]
3. Fabbro, R. Scaling laws for the laser welding process in keyhole mode. *J. Mater. Process. Technol.* **2019**, *264*, 346–351. [CrossRef]
4. Yang, Z.; Tao, W.; Li, L.; Chen, Y.; Shi, C. Numerical simulation of heat transfer and fluid flow during double-sided laser beam welding of t-joints for aluminum aircraft fuselage panels. *Opt. Laser Technol.* **2017**, *91*, 120–129. [CrossRef]
5. Sun, Z.; Kuo, M. Bridging the joint gap with wire feed laser welding. *J. Mater. Process. Technol.* **1999**, *87*, 213–222. [CrossRef]
6. Shi, H.; Zhang, K.; Xu, Z.; Huang, T.; Fan, L.; Bao, W. Applying statistical models optimize the process of multi-pass narrow-gap laser welding with filler wire. *Int. J. Adv. Manuf. Technol.* **2014**, *75*, 279–291. [CrossRef]
7. Chen, G.; Liu, J.; Shu, X.; Gu, H.; Zhang, B.; Feng, J. Beam scanning effect on properties optimization of thick-plate 2a12 aluminum alloy electron-beam welding joints. *Mater. Sci. Eng. A* **2019**, *744*, 583–592. [CrossRef]
8. Pang, S.; Chen, W.; Zhou, J.; Liao, D. Self-consistent modeling of keyhole and weld pool dynamics in tandem dual beam laser welding of aluminum alloy. *J. Mater. Process. Technol.* **2015**, *217*, 131–143. [CrossRef]
9. Matsunawa, A. Problems and solutions in deep penetration laser welding. *Sci. Technol. Weld. Join.* **2001**, *6*, 351–354. [CrossRef]
10. Matsunawa, A.; Mizutani, M.; Katayama, S.; Seto, N. Porosity formation mechanism and its prevention in laser welding. *Weld. Int.* **2003**, *17*, 431–437. [CrossRef]
11. Zhang, M.; Chen, G.; Zhou, Y.; Li, S. Direct observation of keyhole characteristics in deep penetration laser welding with a 10 kW fiber laser. *Opt. Express* **2013**, *21*, 19997–20004. [CrossRef] [PubMed]
12. Li, S.; Chen, G.; Zhang, M.; Zhou, Y.; Zhang, Y. Dynamic keyhole profile during high-power deep-penetration laser welding. *J. Mater. Process. Technol.* **2014**, *214*, 565–570. [CrossRef]
13. Han, S.-W.; Cho, W.-I.; Na, S.-J.; Kim, C.-H. Influence of driving forces on weld pool dynamics in GTA and laser welding. *Weld. World* **2013**, *57*, 257–264. [CrossRef]
14. Rai, R.; Roy, G.G.; DebRoy, T. A computationally efficient model of convective heat transfer and solidification characteristics during keyhole mode laser welding. *J. Appl. Phys.* **2007**, *101*, 054909. [CrossRef]
15. Sohail, M.; Han, S.-W.; Na, S.-J.; Gumenyuk, A.; Rethmeier, M. Characteristics of weld pool behavior in laser welding with various power inputs. *Weld. World* **2014**, *58*, 269–277. [CrossRef]
16. Chang, B.; Allen, C.; Blackburn, J.; Hilton, P.; Du, D. Fluid flow characteristics and porosity behavior in full penetration laser welding of a titanium alloy. *Metall. Mater. Trans. B* **2015**, *46*, 906–918. [CrossRef]
17. Zhao, H.; Niu, W.; Zhang, B.; Lei, Y.; Kodama, M.; Ishide, T. Modelling of keyhole dynamics and porosity formation considering the adaptive keyhole shape and three-phase coupling during deep-penetration laser welding. *J. Phys. D Appl. Phys.* **2011**, *44*, 485302. [CrossRef]
18. Wu, D.; Hua, X.; Li, F.; Huang, L. Understanding of spatter formation in fiber laser welding of 5083 aluminum alloy. *Int. J. Heat Mass Transf.* **2017**, *113*, 730–740. [CrossRef]
19. Wu, D.; Hua, X.; Huang, L.; Zhao, J. Numerical simulation of spatter formation during fiber laser welding of 5083 aluminum alloy at full penetration condition. *Opt. Laser Technol.* **2018**, *100*, 157–164. [CrossRef]
20. Li, X.; Lu, F.; Cui, H.; Tang, X.; Wu, Y. Numerical modeling on the formation process of keyhole-induced porosity for laser welding steel with t-joint. *Int. J. Adv. Manuf. Technol.* **2014**, *72*, 241–254. [CrossRef]

21. Kaplan, A. A model of deep penetration laser welding based on calculation of the keyhole profile. *J. Phys. D Appl. Phys.* **1994**, *27*, 1805–1814. [CrossRef]
22. Semak, V.; Matsunawa, A. The role of recoil pressure in energy balance during laser materials processing. *J. Phys. D Appl. Phys.* **1997**, *30*, 2541–2552. [CrossRef]
23. Kawahito, Y.; Mizutani, M.; Katayama, S. Elucidation of high-power fibre laser welding phenomena of stainless steel and effect of factors on weld geometry. *J. Phys. D Appl. Phys.* **2007**, *40*, 5854–5859. [CrossRef]
24. Fabbro, R. Melt pool and keyhole behaviour analysis for deep penetration laser welding. *J. Phys. D Appl. Phys.* **2010**, *43*, 445501. [CrossRef]